nature nanotechnology

LETTERS

https://doi.org/10.1038/s41565-021-00873-9

Check for updates

Highly anisotropic excitons and multiple phonon bound states in a van der Waals antiferromagnetic insulator

Kyle Hwangbo[1,7], Qi Zhang[1,7], Qianni Jiang[1], Yong Wang[2], Jordan Fonseca[1], Chong Wang[3], Geoffrey M. Diederich[1], Daniel R. Gamelin[4], Di Xiao[3], Jiun-Haw Chu[1], Wang Yao[5] and Xiaodong Xu[1,6] ✉

Two-dimensional (2D) semiconductors enable the investigation of light–matter interactions in low dimensions[1,2]. Yet, the study of elementary photoexcitations in 2D semiconductors with intrinsic magnetic order remains a challenge due to the lack of suitable materials[3,4]. Here, we report the observation of excitons coupled to zigzag antiferromagnetic order in the layered antiferromagnetic insulator $NiPS_3$. The exciton exhibits a narrow photoluminescence linewidth of roughly 350 μeV with near-unity linear polarization. When we reduce the sample thickness from five to two layers, the photoluminescence is suppressed and eventually vanishes for the monolayer. This suppression is consistent with the calculated bandgap of $NiPS_3$, which is highly indirect for both the bilayer and the monolayer[5]. Furthermore, we observe strong linear dichroism (LD) over a broad spectral range. The optical anisotropy axes of LD and of photoluminescence are locked to the zigzag direction. Furthermore, their temperature dependence is reminiscent of the in-plane magnetic susceptibility anisotropy. Hence, our results indicate that LD and photoluminescence could probe the symmetry breaking magnetic order parameter of 2D magnetic materials. In addition, we observe over ten exciton-A_{1g}-phonon bound states on the high-energy side of the exciton resonance, which we interpret as signs of a strong modulation of the ligand-to-metal charge-transfer energy by electron–lattice interactions. Our work establishes $NiPS_3$ as a 2D platform for exploring magneto-exciton physics with strong correlations.

Excitons coupled to magnetic order have been studied in several intrinsic magnetic insulators. For instance, in bulk crystals with Néel antiferromagnetic ordering, Davydov splitting resulting from the coupling of localized excitons in adjacent magnetic ions has been extensively studied[6–9]. Coupling of the electronic structure to magnetic order has also led to strong exciton–magnon coupling[9,10] and drastic tunability of excitonic photoluminescence (PL) by a magnetic field[8]. In quantum well structures, dilute magnetic semiconductors have served as a testbed for exploring magneto-exciton physics. Due to their low spin densities, however, these materials typically show weak inter-ion magnetic interactions and hence uncorrelated spins, posing fundamental limitations for studying physics and applications linked to intrinsic magnetic order[10].

The recent emergence of two-dimensional van der Waals (vdW) magnets may provide a new quantum well platform with intrinsic magnetic order[11,12]. Indeed, localized excitons with spontaneous circularly polarized PL have been observed in ferromagnetic monolayer CrI_3 and $CrBr_3$ (refs. [4,13]). The first-principles calculations for CrI_3 suggest that the ground state exciton is dark and Frenkel type[14]. The Frenkel character of the ground state exciton makes it insensitive to layer thickness[4], and thus not suitable for vdW engineering of exciton properties (for example, moiré excitons). Furthermore, the PL linewidth of the ground state exciton is broad (roughly 150 meV), while narrow linewidth is desirable for magneto-optical physics. Last, there is little known about excitons in 2D antiferromagnets with Néel and zigzag type. There is no net magnetic moment in antiferromagnets, and the strong exchange interactions often require high magnetic fields to tune the magnetic order. Therefore, it is unknown how excitons are coupled to these antiferromagnetic orders at the atomically thin limit.

$NiPS_3$ belongs to a class of transition metal phosphorous trichalcogenides (APX_3, A:Fe, Mn, Ni and X:S, Se), which are vdW antiferromagnetic insulators[15–19]. Within individual $NiPS_3$ layers, Ni is arranged in a honeycomb lattice structure. The spins are aligned in the zigzag direction along the *a* axis, while the adjacent spin chains are anti-aligned (Fig. 1a), forming a zigzag antiferromagnetic order. Neutron scattering suggests that the spins are mostly aligned in-plane with only a slight tilt out of plane[19,20]. The interlayer coupling between adjacent layers is ferromagnetic (Fig. 1a). On the basis of Raman scattering measurements, long-range magnetic order remains down to the bilayer, but is suppressed in monolayers[21]. X-ray absorption studies suggest that $NiPS_3$ is a charge-transfer antiferromagnetic insulator that exhibits strong correlation effects[22].

We perform both PL and optical reflection spectroscopy measurements on $NiPS_3$ samples with varying thicknesses, down to a monolayer (Methods). Figure 1b is an optical microscope image of a representative sample with the layer numbers indicated in Fig. 1c. We first present linear polarization-resolved PL measurements of a thin bulk crystal. The horizontal and vertical axes are defined according to polarization-resolved Raman spectroscopy (Extended Data Fig. 1)[21,23]. Figure 1d shows the data at selected temperatures. Notably, at 15 K, a pronounced peak with a Lorentzian lineshape is observed at 840.5 nm (1.4753 eV); this is a signature of exciton

[1]Department of Physics, University of Washington, Seattle, WA, USA. [2]School of Physics, Nankai University, Tianjin, China. [3]Department of Physics, Carnegie Mellon University, Pittsburgh, PA, USA. [4]Department of Chemistry, University of Washington, Seattle, WA, USA. [5]Department of Physics and Center of Theoretical and Computational Physics, University of Hong Kong, Hong Kong, China. [6]Department of Materials Science and Engineering, University of Washington, Seattle, WA, USA. [7]These authors contributed equally: Kyle Hwangbo, Qi Zhang. ✉e-mail: xuxd@uw.edu

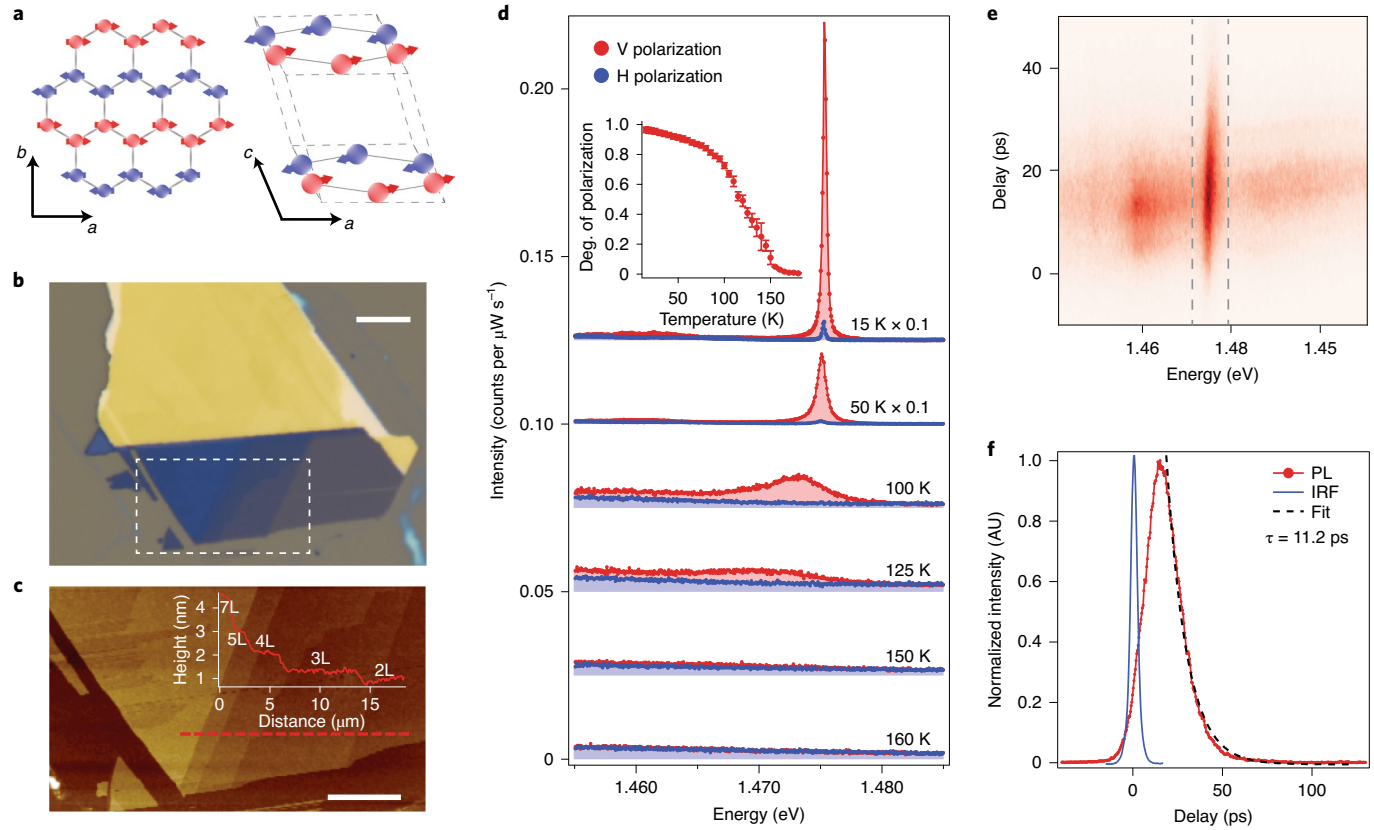

Fig. 1 | Anisotropic antiferromagnetic excitons in thin bulk $NiPS_3$ crystal. a, Schematic of zigzag antiferromagnetic order in a single layer of $NiPS_3$ and of monoclinic stacking with ferromagnetic interlayer coupling in a bulk crystal. **b**, Optical microscope image of exfoliated samples. Scale bar, 10 μm. **c**, Atomic force microscopy image of the area enclosed by the dashed rectangle in **b**. Scale bar, 10 μm. Layer numbers are indicated. **d**, Linear polarization-resolved PL of a thin bulk $NiPS_3$ excited with 633 nm light at selected temperatures. Blue and red data represent horizontally (H) and vertically (V) polarized detection. Inset: the degree of linear polarization as a function of temperature. Error bars were obtained from a Lorentzian fit of the PL signals. **e**, Raw streak camera image of time-resolved PL at 5 K. **f**, Integrated intensity time trace (red curve) of the area enclosed by the dashed lines in **e**. Blue curve is the measured instrument response function. The exciton lifetime of roughly 11 ps was extracted by fitting the time trace with a monoexponential function.

PL. The peak full-width at half-maximum is as narrow as 0.20 nm (350 μeV) (Fig. 1d), which is much narrower than the peak widths measured in 2D transition metal dichalcogenides encapsulated in hexagonal boron nitride[24,25]. Although the exact band edge of $NiPS_3$ and the exciton binding energy are unknown, the optical bandgap has been identified at 1.8 eV (refs. [5,22]). Figure 1e shows the PL intensity plot as a function of energy and time. By integrating the detected intensity over wavelength within the region of interest, we obtain the time trace of the PL in Fig. 1f. The fitting of the PL time trace with a monoexponential function yields exciton lifetime to be about 11 ps. This corresponds to an intrinsic linewidth of 30 μeV, smaller than the measured linewidth of about 350 μeV. This comparison shows that the narrow exciton PL linewidth is dominated by pure dephasing or inhomogeneous broadening.

As shown in Fig. 1d, the exciton PL is highly anisotropic with the degree of linear polarization, $\rho = \frac{I_\perp - I_\parallel}{I_\perp + I_\parallel}$, approaching unity (0.96). Here, $I_\parallel$ ($I_\perp$) is the peak intensity of horizontally (vertically) polarized PL. This observation provides an indication that the exciton couples strongly to the zigzag antiferromagnetic order. Even though the three-fold rotational symmetry is already broken by the monoclinic layer stacking, the observed optical anisotropy is of a purely magnetic origin, as we will discuss below. We have also performed polarization-dependent excitation and unpolarized detection measurements. These measurements show that PL has little dependence on the excitation polarization (Extended Data Fig. 2).

The strong exciton-magnetic order coupling is corroborated by the temperature-dependent PL (Extended Data Fig. 3). As temperature increases, the PL intensity drops while the peak width broadens (Fig. 1d). Above 100 K, the exciton emission loses its Lorentzian lineshape and becomes increasingly broad as the temperature approaches the Néel temperature (T_N), nearly vanishing above T_N of 150 K (ref. [15]). Although thermal disassociation and phonon effects are the primary factors that influence the temperature-dependent PL linewidth and intensity, enhanced spin fluctuations and changes in the electronic structure near T_N could contribute as well. There is also an overall concomitant red shift of the exciton peak as temperature increases, consistent with the reduced bandgap from lattice warming effects. Notably, the PL remains strongly linearly polarized up to about 70 K, but the degree of polarization decreases and eventually vanishes above T_N (inset of Fig. 1d). The exciton linear polarization dependence on temperature resembles the in-plane magnetic susceptibility anisotropy, pointing to an intimate connection between the two (Extended Data Fig. 4).

Figure 2a shows the PL as a function of layer number at 15 K. The exciton luminescence can be clearly observed down to bilayer, but not appreciable in monolayers. Figure 2b shows the PL mapping of the sample area highlighted in Fig. 1b, where the seven- and four-layer regions are bright while the adjacent, thinner layers are barely visible. Furthermore, the PL peak blue shifts relative to the bulk PL peak as the layer number decreases (Fig. 2c). All these effects manifest most strongly in the transition from trilayer to bilayer.

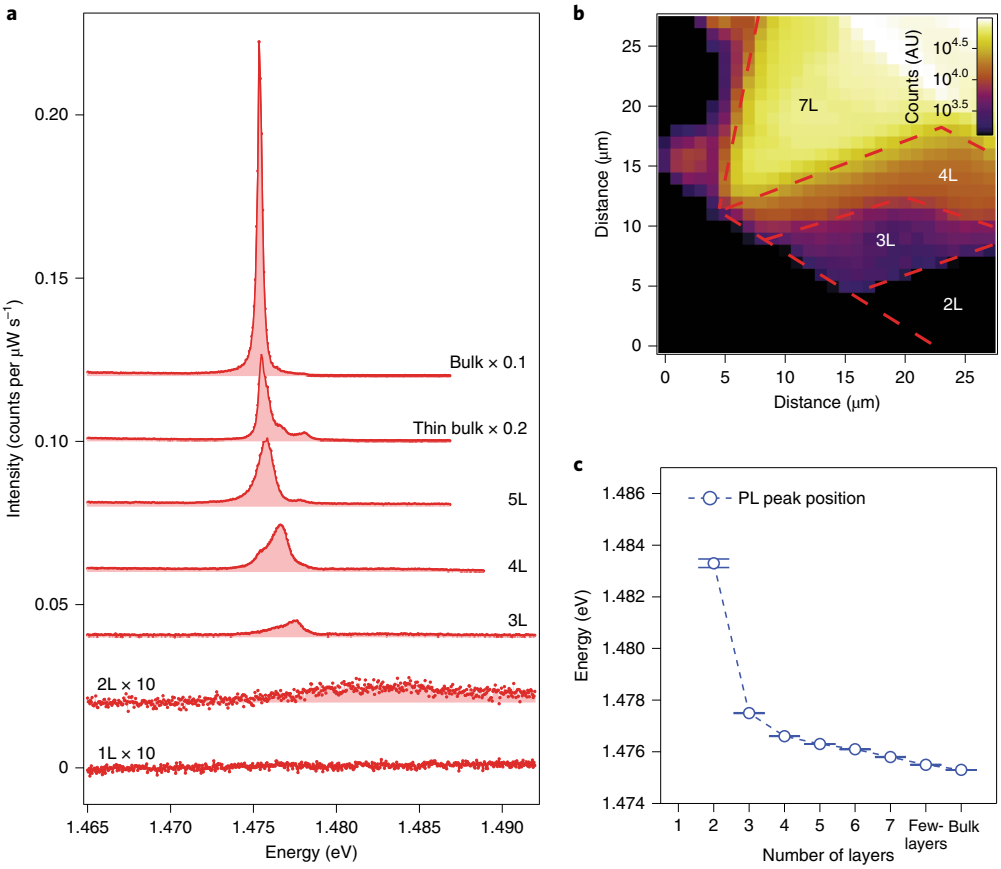

Fig. 2 | Thickness-dependent exciton luminescence and electronic structure. a, Exciton PL as a function of layer number. Both excitation and detection are vertically polarized. **b**, PL intensity map of the area enclosed by the white dashed box in Fig. 1b. **c**, Extracted peak energy position versus layer number. Error bars were obtained from a Lorentzian fit of the PL signals.

The observation of thickness-dependent PL indicates layer-dependent electronic structures. We have performed a first-principles band-structure calculation from monolayer to six layers (Extended Data Fig. 5). The calculation shows that the valence band maximum lies between the Γ and X points of the Brillouin zone. In trilayer and above, the conduction band minimum (CBM) also lies in this region, although it rests closer to the Γ point, making the interband transition indirect with a relatively small CBM-valence band maximum crystal momentum separation. By contrast, in bilayer and monolayer, the CBM moves to the Y point, drastically increasing the momentum separation of the indirect bandgap. Furthermore, the calculation shows an increased bandgap as the layer number decreases. Both of these theoretical features are corroborated by our data. The increase in crystal momentum separation of the interband transition explains the reduction in PL intensity with decreasing thickness, particularly going from trilayer to bilayer. The increased bandgap in thinner flakes explains the observed blue shift of the PL peaks. Our calculation is consistent with a recent prediction on layer-dependent electronic structure in $NiPS_3$ (ref. [5]). The observed, sensitive dependence of excitonic PL on the evolution of band structure versus layer number points to the Wannier-like character of the exciton wavefunction.

The PL linewidth broadens slightly from five-layer to trilayer but increases by a factor of ten from trilayer to bilayer. This sudden linewidth increase cannot be explained solely by an increased sensitivity to the substrate in the atomically thin limit. In fact, samples with and without hBN encapsulation do not show any appreciable differences in the linewidth (Extended Data Fig. 6). We speculate that the enhanced spin fluctuations in the atomically thin limit[26] may contribute to the linewidth broadening in bilayer.

The exciton PL in atomically thin flakes remains highly linearly polarized. We use a five-layer sample to illustrate this property, due to its strong PL. Figure 3a shows the polarization-resolved PL (see Extended Data Fig. 6 for thinner samples). As in thin bulk crystals, the PL is polarized along the vertical axis with a near unity ρ, again pointing towards strong coupling of the exciton to the zigzag antiferromagnetic order (Fig. 3b). Figure 3c plots the temperature-dependent PL with vertically polarized detection (see Extended Data Fig. 7 for extracted linewidth and intensity). The peak intensity first reduces slowly as temperature increases, but then quickly drops as the temperature rises above 40 K and is barely visible above 100 K. The degree of linear polarization has similar temperature dependence (Fig. 3d). The exact cause of the disappearance of the PL signal in the five-layer at a temperature lower than that in thin bulk crystal is not clear. The data show that, for atomically thin flakes, linearly polarized PL measurements can be used to study the zigzag antiferromagnetic order and the associated optical anisotropy, but they have a limitation in probing the temperature-dependent magnetic properties, especially near T_N.

In addition to PL measurements, we perform linear polarization-resolved optical reflection measurements. We define linear dichroism (LD) as $\frac{R_\perp - R_\parallel}{R_\perp + R_\parallel}$, where $R_\parallel$ ($R_\perp$) is the peak intensity of horizontally (vertically) polarized optical reflection. Figure 4a shows a broad LD spectrum from a thin bulk sample. The LD is clearly enhanced at charge-transfer exciton resonances (for example,

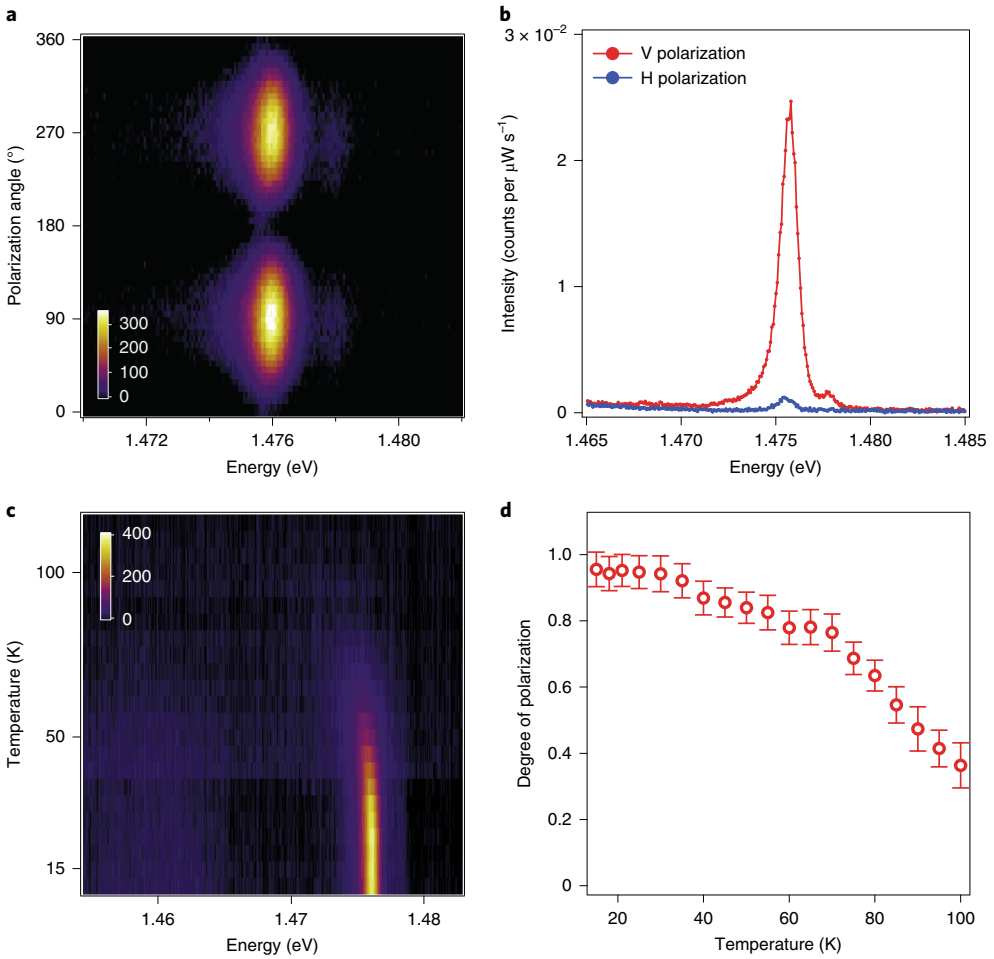

Fig. 3 | Exciton-zigzag antiferromagnetic order coupling in a five-layer sample. a, PL intensity plot as a function of linear polarization detection angle. **b**, Horizontally (H) and vertically (V) polarized PL spectra. **c**, Temperature-dependent PL with covertically polarized excitation and detection. **d**, Degree of linear polarization versus temperature. Error bars were obtained from a Lorentzian fit of the PL signals.

at 2.2 eV, ref. [22]). In addition to these broad peaks, there is a sharp resonance at 838 nm (or 1.480 eV), about 5 meV above the anisotropic exciton observed in the PL. The lineshape of the peak results from the combination of thin film interference and a nearby state with weaker anisotropy (Extended Data Fig. 8).

LD shares a similar temperature-dependent behaviour with the PL degree of polarization. As shown in the inset of Fig. 4a, LD first decreases slowly as the temperature increases, then drops drastically near T_N and vanishes above it. In addition, the LD axis is along the same optical anisotropy axis as PL and Raman scattering (Extended Data Fig. 1). These results further support the fact that both LD and linearly polarized exciton PL originate from the zigzag antiferromagnetic order, which breaks three-fold rotation symmetry (Extended Data Fig. 5). Both LD and PL also have little dependence on out-of-plane magnetic field up to 9 T, consistent with the strong antiferromagnetic exchange interactions[19,20] (Extended Data Fig. 9). Note that PL linear polarization is much larger than LD. This discrepancy is due to the fact that LD is measured on top of a strong unpolarized reflection background, while exciton PL is nearly background free.

On the high-energy side of the sharp exciton peak, there are over ten oscillation features with a period of about 28 meV (Fig. 4b). These features vanish on bare SiO_2:Si substrate, which rules out artefacts from the experimental setup. Moreover, the oscillation period is independent of the sample thickness, precluding simple interference effects. Instead, these spectral structures are probably exciton–phonon bound states[26,27]. Such states have previously been observed in molecular crystals[28]. The energy separation between the exciton and the bound states is usually 10–20% smaller than the corresponding phonon energy[26–29]. By examining the Raman spectrum (Extended Data Fig. 1), we find the A_{1g} phonon mode at 32 meV (258 cm^{-1}) to be the most likely candidate bound to the exciton.

Compared to exciton–phonon bound states observed in various bulk crystals, there are several unique aspects of our observation. First, usually only one or up to a few exciton–phonon bound states are observed in reported systems[26–28]. Here, we observe over ten states, signifying an exceptionally strong exciton–phonon coupling. Furthermore, $NiPS_3$ is a charge-transfer insulator where the nickel 3*d* orbitals and sulfur *p* orbitals form a ligand field charge-transfer transition. The involved A_{1g} phonon represents the out-of-plane motion of the S atoms (Fig. 4f). Such a motion would modify the S-Ni bond. Therefore, the data indicate that the A_{1g} mode strongly modifies the charge-transfer energy, and thus the electronic structure of the crystal. This observation, as well as the strong thickness dependence of the PL intensity, indicates that the observed exciton is not a Frenkel exciton localized in the Ni^{2+} cation[30,31].

Second, the exciton–phonon bound states can be observed down to the atomically thin limit. Figure 4c shows the LD spectra versus the layer number. Excitons with associated A_{1g} phonon bound states can be clearly resolved down to trilayers. However, the signal becomes too weak to resolve in bilayers and monolayers.

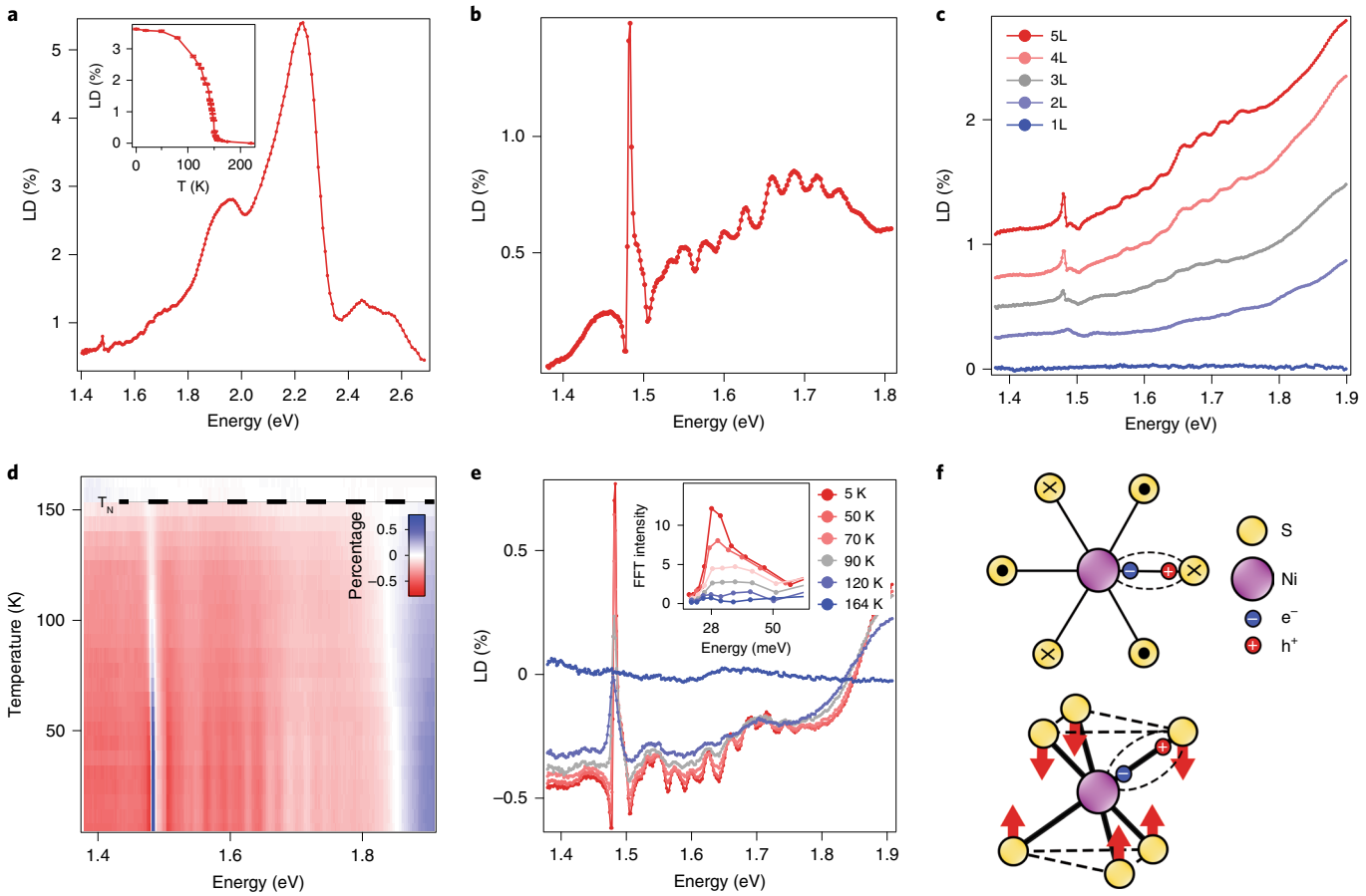

Fig. 4 | Multiple exciton–phonon bound states. a, LD spectrum of a thin bulk flake. Data are taken at 5 K. Inset: temperature-dependent LD extracted at a photon energy of 2.17 eV. Error bars were obtained from a sinusoidal fit of the rotational LD measurements. **b**, Low energy zoom in LD spectrum. **c**, LD versus layer number at an atomically thin limit. Data are taken at 5 K. **d**, LD intensity plot as a function of temperature and photon energy. **e**, LD spectra at selected temperatures. Inset shows the corresponding Fourier transformation of LD spectra. **f**, Cartoon of exciton–phonon coupling via A_{1g}-mode modulated ligand field transition. Direction of vibrational motion of S atoms depicted with in-to-figure (cross) and out-of-figure (black spot) symbols.

Note that the oscillation amplitude appears to be larger for higher-order bound states. This is consistent with the fact that higher-order bound states involve more phonons and thus larger anisotropy, yielding a larger LD signal than the lower-order ones.

Last, the exciton–phonon bound states strongly couple to the magnetic order. Figure 4d shows the LD intensity plot as a function of temperature and photon energy. The exciton–phonon bound states are evident below T_N. The LD amplitude of the bound states decreases as the temperature increases. This observation is highlighted by the LD spectra at selected temperatures (Fig. 4e). The corresponding Fourier transform of the data is plotted in the inset. The oscillation amplitude vanishes above T_N, consistent with the exciton's strong coupling to the zigzag antiferromagnetic order. The oscillation frequency shows a slight blue shift as temperature increases, signifying the weakening of the exciton–phonon binding.

Our work reveals that $NiPS_3$ hosts excitons that are highly anisotropic with the optical anisotropy axis determined by the zigzag antiferromagnetic order. The demonstrated optical anisotropy measurements thus provide a new optical means to study a broad class of rotational-symmetry-breaking antiferromagnetic orders in correlated materials, such as zigzag or stripe antiferromagnetism. These excitons also exhibit strong dependence on the layer number, which originates from layer-dependent electronic structure. Additionally, the exciton in $NiPS_3$ is Wannier-like, which makes $NiPS_3$ amenable to band-structure engineering via stacking into twisted homobilayers and moiré heterostructures with different vdW materials. We thus foresee that $NiPS_3$ can be useful for engineering magnetic moiré excitons and exploring excitonic many-body quantum states. Last, exceptionally strong exciton–phonon coupling points to the possibility of strong exciton–magnon coupling as well as tuning magnetic order and correlated effects in $NiPS_3$ via optical manipulation of lattice degree of freedom.

Online content

Any methods, additional references, Nature Research reporting summaries, source data, extended data, supplementary information, acknowledgements, peer review information; details of author contributions and competing interests; and statements of data and code availability are available at https://doi.org/10.1038/s41565-021-00873-9.

Received: 21 July 2020; Accepted: 3 February 2021;
Published online: 11 March 2021

References

1. Schmitt-Rink, S. et al. Linear and nonlinear optical properties of semiconductor quantum wells. *Adv. Phys.* **38**, 89–188 (1989).
2. Mak, K. F. & Shan, J. Photonics and optoelectronics of 2D semiconductor transition metal dichalcogenides. *Nat. Photonics* **10**, 216–226 (2016).
3. Burch, K. S. et al. Magnetism in two-dimensional van der Waals materials. *Nature* **563**, 47–52 (2018).
4. Seyler, K. L. et al. Ligand-field helical luminescence in a 2D ferromagnetic insulator. *Nat. Phys.* **14**, 277–281 (2018).

5. Lane, C. & Zhu, J.-X. Thickness dependence of electronic structure and optical properties of a correlated van der Waals antiferromagnetic $NiPS_3$ thin film. *Phys. Rev. B.* **102**, 075124 (2020).
6. Togashi, H. et al. Field-induced Davydov splitting of excitons in quasi-one-dimensional antiferromagnet $CsMnCl_3{\cdot}2H_2O$. *J. Phys. Soc. Jpn* **57**, 353–360 (1988).
7. van der Ziel, J. P. Davydov splitting of the 2E lines in antiferromagnetic Cr_2O_3. *Phys. Rev. Lett.* **18**, 237–239 (1967).
8. Heiss, W. et al. Giant tunability of exciton photoluminescence emission in antiferromagnetic EuTe. *Phys. Rev. B.* **63**, 165323 (2001).
9. Gnatchenko, S. L. et al. Exciton-magnon structure of the optical absorption spectrum of antiferromagnetic $MnPS_3$. *Low. Temp. Phys.* **37**, 144–148 (2011).
10. Gaj, J. A. & Kossut, J. *Introduction to the Physics of Diluted Magnetic Semiconductors* Springer Series in Materials Science Vol. 144 (Springer, 2010).
11. Huang, B. et al. Layer-dependent ferromagnetism in a van der Waals crystal down to the monolayer limit. *Nature* **546**, 270–273 (2017).
12. Gong, C. et al. Discovery of intrinsic ferromagnetism in two-dimensional van der Waals crystals. *Nature* **546**, 265–269 (2017).
13. Zhang, Z. et al. Direct photoluminescence probing of ferromagnetism in monolayer two-dimensional $CrBr_3$. *Nano Lett.* **19**, 3138–3142 (2019).
14. Wu, M. et al. Physical origin of giant excitonic and magneto-optical responses in two-dimensional ferromagnetic insulators. *Nat. Commun.* **10**, 2371 (2019).
15. Le Flem, G. et al. Magnetic interactions in the layer compounds MPX3 (M = Mn, Fe, Ni; X = S, Se). *J. Phys. Chem. Solids* **43**, 455–461 (1982).
16. Chittari, B. L. et al. Electronic and magnetic properties of single-layer MPX3 metal phosphorous trichalcogenides. *Phys. Rev. B.* **94**, 184428 (2016).
17. Lee, J.-U. et al. Ising-type magnetic ordering in atomically thin $FePS_3$. *Nano Lett.* **16**, 7433–7438 (2016).
18. Wang, X. et al. Raman spectroscopy of atomically thin two-dimensional magnetic iron phosphorus trisulfide ($FePS_3$) crystals. *2D Mater.* **3**, 031009 (2016).
19. Wildes, A. R. et al. Magnetic structure of the quasi-two-dimensional antiferromagnet $NiPS_3$. *Phys. Rev. B.* **92**, 224408 (2015).
20. Lançon, D. et al. Magnetic exchange parameters and anisotropy of the quasi-two-dimensional antiferromagnet $NiPS_3$. *Phys. Rev. B.* **98**, 134414 (2018).
21. Kim, K. et al. Suppression of magnetic ordering in XXZ-type antiferromagnetic monolayer $NiPS_3$. *Nat. Commun.* **10**, 345 (2019).
22. Kim, S. Y. et al. Charge-spin correlation in van der Waals antiferromagnet $NiPS_3$. *Phys. Rev. Lett.* **120**, 136402 (2018).
23. Kuo, C.-T. et al. Exfoliation and Raman spectroscopic fingerprint of few-layer $NiPS_3$ van der Waals crystals. *Sci. Rep.* **6**, 20904 (2016).
24. Cadiz, F. et al. Excitonic linewidth approaching the homogeneous limit in MoS_2 based van der Waals heterostructures. *Phys. Rev. X.* **7**, 021026 (2017).
25. Wierzbowski, J. et al. Direct exciton emission from atomically thin transition metal dichalcogenide heterostructures near the lifetime limit. *Sci. Rep.* **7**, 12383 (2017).
26. Toyozawa, Y. & Hermanson, J. Exciton-phonon bound state: a new quasiparticle. *Phys. Rev. Lett.* **21**, 1637 (1968).
27. Merlin, R. et al. Multiphonon processes in YbS. *Phys. Rev. B.* **17**, 4951 (1978).
28. Levinson, Y. B. & Rashba, E. I. Electron-phonon and exciton-phonon bound states. *Rep. Prog. Phys.* **36**, 1499 (1973).
29. Liang, W. Y. & Yoffe, A. D. Transmission spectra of ZnO single crystals. *Phys. Rev. Lett.* **20**, 59 (1968).
30. Banda, E. J. K. B. Optical absorption of $NiPS_3$ in the near-infrared, visible and near-ultraviolet regions. *J. Phys. C.: Solid State Phys.* **19**, 7329 (1986).
31. Piacentini, M. et al. Optical transitions, XPS, electronic states in $NiPS_3$. *Chem. Phys.* **65**, 289 (1982).

Methods

Crystal growth and sample fabrication. Single crystals of $NiPS_3$ were synthesized by chemical vapour transport method using iodine as the transport agent. Stoichiometric amounts of nickel powder (99.998%), phosphorous powder (98.9%) and sulfur pieces (99.9995%) were mixed with iodine (1 mg cm^{-3}) and sealed in quartz tubes (10 cm in length) under high vacuum. The tubes were placed in a horizontal one-zone tube furnace with the charge near the centre of the furnace. Sizeable crystals were obtained after gradually heating the precursor up to 950 °C, staying there for 1 week and then cooling down to room temperature. The crystals were then exfoliated onto (90 nm) SiO_2:Si substrate in an Argon gas protected glove box. The layer thickness was identified by atomic force microscopy imaging in the glove box as well as by optical contrast analysis. To protect the samples from degrading in ambient conditions, the samples were sealed in a copper sample holder under a transparent cover slip inside the glove box before being transported and loaded into the cryostat. The total time the sealed sample spent outside of the glove box before the loading was usually less than 10 min.

PL and Raman measurement. A HeNe laser (633 nm) was used to excite the $NiPS_3$ sample, which was placed in a closed cycle cryostat with temperature range from 5 to 300 K. Both PL and Raman measurements were polarization-resolved and collected by a spectrometer with a liquid nitrogen cooled CCD camera. A magnetic field up to 9 T was applied in Faraday geometry.

LD spectroscopy. The measurements were carried out in the reflection geometry. A supercontinuum laser with a filter set was used as a tuneable light source with a spectral resolution of 1 nm. The laser beam was double modulated by a photoelastic modulator with maximum half-wave retardance and a mechanical chopper. After phase modulation, the light passed through a half-waveplate, and then was focused down onto the sample at normal incidence with an objective lens. A laser power of 5 μW was used. The reflected light was detected by a photodiode, and further demodulated at 100 and 1 kHz, which corresponds to the photoelastic modulator linear polarization modulation and the chopper modulation frequency, respectively.

Band-structure calculation. The Quantum Espresso package[32] was used to perform to the first-principles calculations by taking the Rappe–Rabe–Kaxiras–Joannopoulos ultrasoft pseudoptentials for the semilocal Perdew–Burke–Ernzerhof generalized gradient approximation (GGA) and the vdW-D2 correction. The crystal structures were relaxed with the convergence threshold 10^{-4} Ry for total energy and 10^{-4} Ry per Bohr for force. The $6\times3\times1$ Monkhorst–Pack grids were used to sample the k points during the self-consistency calculation for the ground state electron structure, which converges below the criterion 10^{-7} Ry for total energy. The electron correlation effect was taken into account by the GGA + U method by setting $U = 6.45$ eV (ref. [16]).

Time-resolved PL measurements. Time-resolved PL measurements were conducted using a streak camera (Hamamatsu-C10910) synchronized with an oscillator (Coherent-Mira 900-F). Laser pulses from the oscillator with a central wavelength of 820 nm and temporal width of roughly 150 fs were used to pump a non-linear photonic crystal fibre (NKT Photonics-FemtoWhite 800) to generate supercontinuum pulses. Several bandpass filters were then used to centre the excitation bandwidth around 633 nm. The excitation was focused by an objective lens onto the sample, which was held at 5 K by a closed cycle cryostat (Attocube-Attodry 2100). The PL signal was spectrally and temporally dispersed within the streak camera and detected on the internal CCD. Since the measured instrument response function was substantially shorter than the PL time trace, the exciton lifetime was obtained by fitting the time trace with a monoexponential function.

Data availability

All other data that support the plots within this paper and other findings of this study are available from the corresponding author upon reasonable request. Source data are provided with this paper.

References

32. Giannozzi, P. et al. QUANTUM ESPRESSO: a modular and open-source software project for quantum simulations of materials. *J. Phys.: Condens. Matter* **21**, 395502 (2009).

Acknowledgements

This work was mainly supported by the Department of Energy, Basic Energy Sciences, Materials Sciences and Engineering Division (DE-SC0012509 and DE-SC0018171). Device fabrication and part of PL measurement were supported by Air Force Office of Scientific Research Multidisciplinary University Research Initiative program, grant no. FA9550-19-1-0390. Bulk crystal growth is supported by grant no. NSF MRSEC DMR-1719797 and the Gordon and Betty Moore Foundation's EPiQS Initiative, grant no. GBMF6759 to J.H.C. Y.W. is supported by NSFC Projects (grant nos. 61674083 and 11604162). We also acknowledge the use of the facilities and instrumentation supported by grant no. NSF MRSEC DMR-1719797. X.X. and J.H.C. acknowledge the support from the State of Washington funded Clean Energy Institute.

Author contributions

X.X., Q.Z. and K.H. conceived the experiment. K.H. and Q.Z. fabricated samples and performed optical measurements, assisted by J.F. and G.M.D. All authors contributed to the data analysis and interpretation. Y.W. and W.Y. performed band-structure calculation. C.W. and D.X. calculated the optical anisotropy. Q.J. and J.-H.C. synthesized and characterized the bulk crystals. K.H., Q.Z., X.X. and J.F. wrote the paper with input from all authors. All authors discussed the results and commented on the manuscript.

Competing interests

The authors declare no competing interests.

Additional information

Extended data is available for this paper at https://doi.org/10.1038/s41565-021-00873-9.

Supplementary information The online version contains supplementary material available at https://doi.org/10.1038/s41565-021-00873-9.

Correspondence and requests for materials should be addressed to X.X.

Peer review information *Nature Nanotechnology* thanks the anonymous reviewers for their contribution to the peer review of this work.

Reprints and permissions information is available at www.nature.com/reprints.

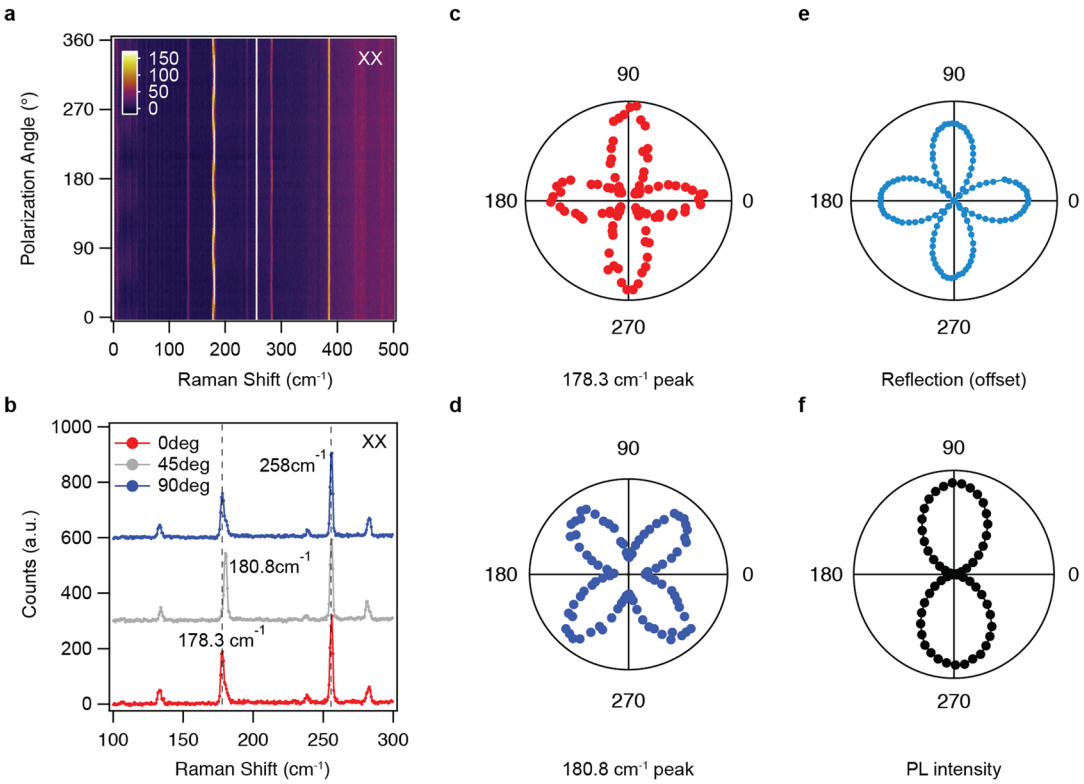

Extended Data Fig. 1 | Polarization-resolved Raman spectroscopy, optical reflection and photoluminescence measurements of the same thin-bulk $NiPS_3$ flake. a, Co-linearly polarized Raman scattering (the XX channel). **b**, Raman spectra at 0°, 45°, and 90° of linear polarization. **c**, Polar plot of 178.3 cm^{-1}, and **d**, 180.8 cm^{-1} Raman mode intensity as function of linear polarization angle. Data is taken at 15 K. **e**, Offset optical reflection at 633 nm as function of linear polarization angle. The positive lobes indicate the high reflection direction. **f**, Polar plot of photoluminescence intensity as a function of linear polarization detection angle. Near unity linearly polarized photoluminescence is observed along the vertical direction. Horizontal (H) and vertical (V) polarization direction is defined along 0° and 90° in this figure, respectively.

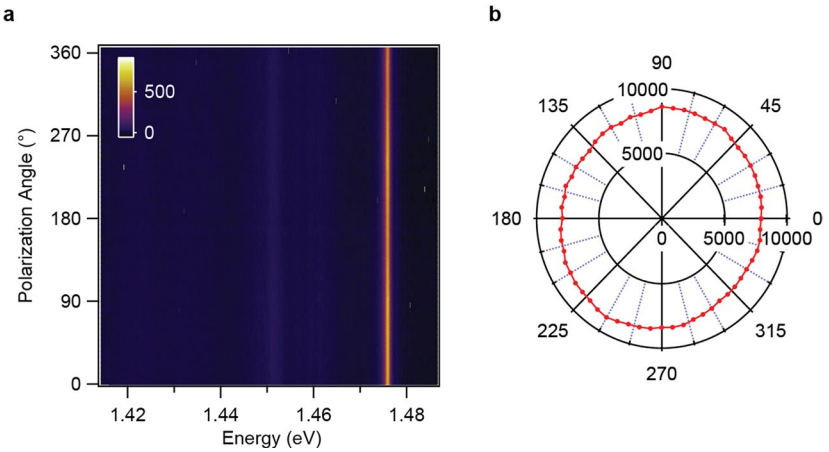

Extended Data Fig. 2 | Photoluminescence as a function of excitation linear polarization angle. a, Photoluminescence intensity plot as a function of photon energy and excitation polarization. Detection is unpolarized. **b**, Polar plot of peak intensity vs excitation polarization.

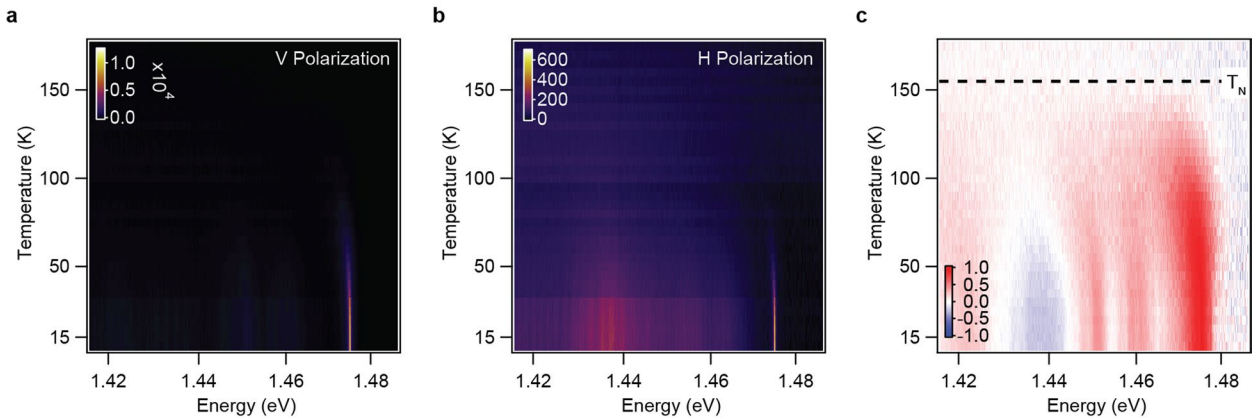

Extended Data Fig. 3 | Temperature- and polarization-resolved photoluminescence from a bulk NiPS3 flake. The excitation laser is at 633 nm and vertically polarized. Photoluminescence intensity plot with **a**, vertically and **b**, horizontally polarized detection. The main excitonic peak is strongly linearly polarized. There are low energy and very weak photoluminescence features. These states are more visible in **c**, temperature dependent degree of linear polarization plot. The first three features have energy separation of about 10 ~ 12 meV, implying that the two low energy features are phonon replica of the exciton. The feature at 1.44 eV has stronger photoluminescence intensity than the first two while having opposite polarization, indicating that it has a different origin from the first two. We speculate that this state may arise from the electric dipole forbidden *d-d* transitions localized in the Ni^{2+}. The identification of the exact origin of these states requires future efforts.

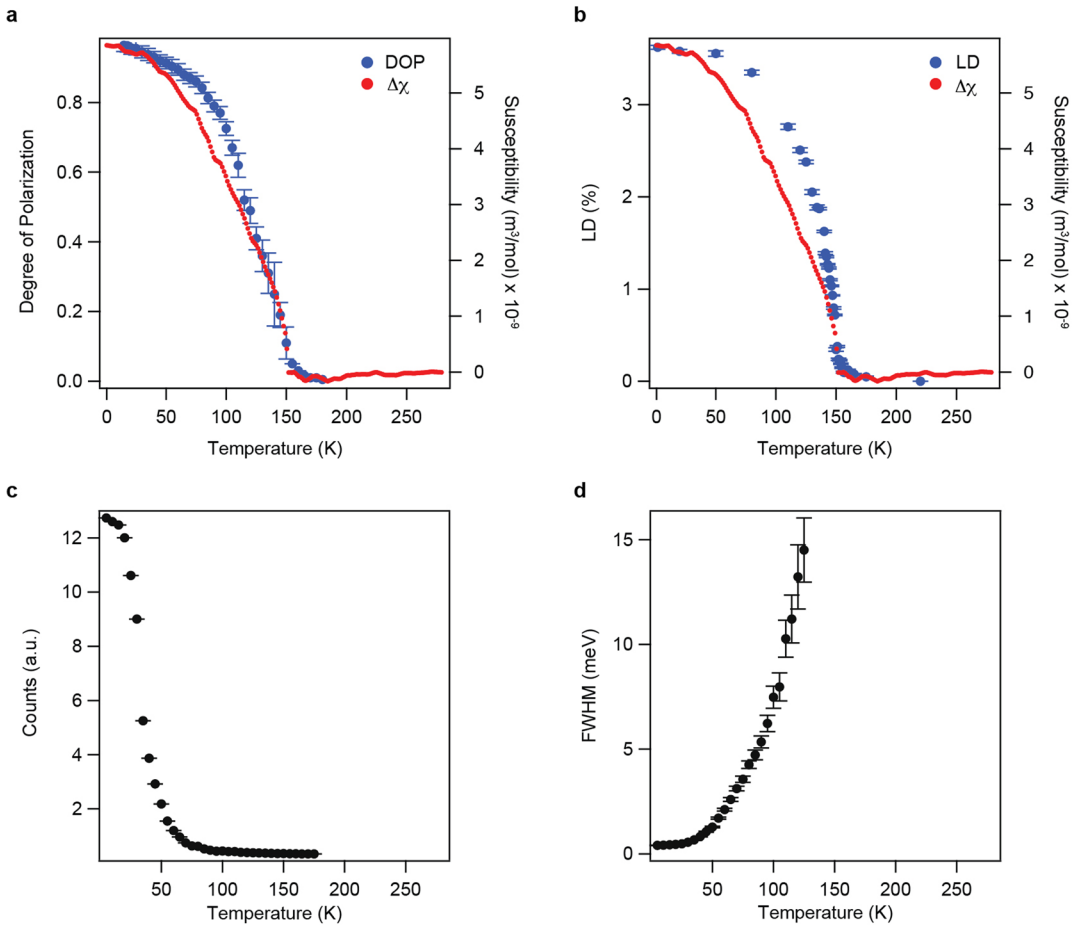

Extended Data Fig. 4 | Comparison of temperature dependent exciton photoluminescence properties with in-plane magnetic susceptibility anisotropy $\Delta\chi$. $\Delta\chi$ is the magnetic susceptibility difference between *a* and *b* axes of bulk crystal $NiPS_3$, extracted from ref. [19]. The photoluminescence measurements are done on the sample presented in Fig. 1e in the main text. **a** and **b** overlays $\Delta\chi$ (red) with degree of linear polarization (DOP, blue) and linear dichroism (LD, blue) as a function of temperature, respectively. The temperature dependent behavior of DOP and LD resembles that of $\Delta\chi$, supporting the in-plane magnetic susceptibility anisotropy as their cause. Error bars for DOP were obtained from a Lorentzian fit of the PL signals. Temperature dependent **c**, photoluminescence intensity and **d**, full width at half maximum (FWHM). FWHM is not shown above 120 K as the peak shape was not suitable for fitting. Error bars in **c** and **d** signify the confidence bounds of a Lorentzian fit.

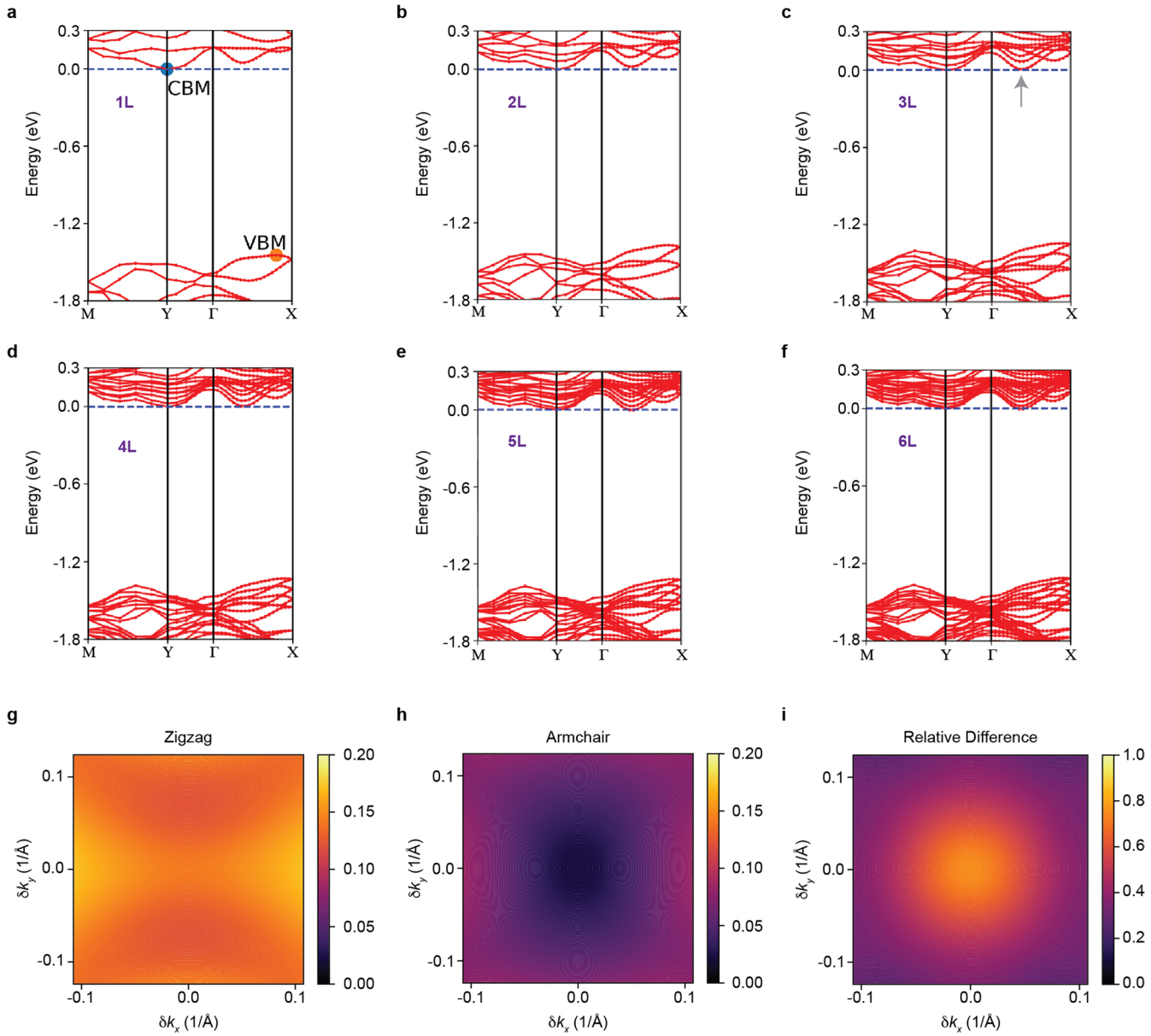

Extended Data Fig. 5 | DFT calculated band structure and oscillator strength of inter-band optical transition. a–f, layer number dependent band structure. The rectangular unit cell and Brillouin zone have been exploited during the calculations. The k path for the band is along M-Y-Γ-X, where Γ = (0,0), X = (π/a,0),Y=(0, π/b), M = (π/a,π/b). The zero energy has been set to the conduction band minimum at Y point for comparison. The highest energy valence band is near the X point, indicated in the figure. We can see that while the lowest energy conduction band is at Y point in monolayer and bilayer, an energy minimum between Γ and X, indicated by the arrow in the trilayer band structure, appears as the layer number increases to 3 and above. Therefore, $NiPS_3$ experiences a transition from indirect in monolayer and bilayer to less indirect bandgap in trilayer and above. This transition is likely responsible for the observed layer thickness dependent exciton photoluminescence, which manifest most strongly between trilayer and bilayer. **g–i**, Oscillator strength along the zigzag (*a*) and armchair (*b*) direction in the vicinity of the X point. We have averaged the oscillator strength over the quasi-degenerate bands near the band edges, that is, $\frac{1}{32}\sum_{v,c}|\langle ck|\hat{v}|vk\rangle|^2$, where *v* runs over the 4 near degenerate valence bands and *c* runs over 8 nearly degenerate conduction bands. The unit of the averaged velocity matrix elements is $(eV \cdot Å)^2$. The large difference of the oscillator strength between zigzag and armchair, that is (zigzag-armchair)/(zigzag+armchair), represents highly anisotropic states due to the zigzag antiferromagnetic order. This is consistent with the observed exciton LD.

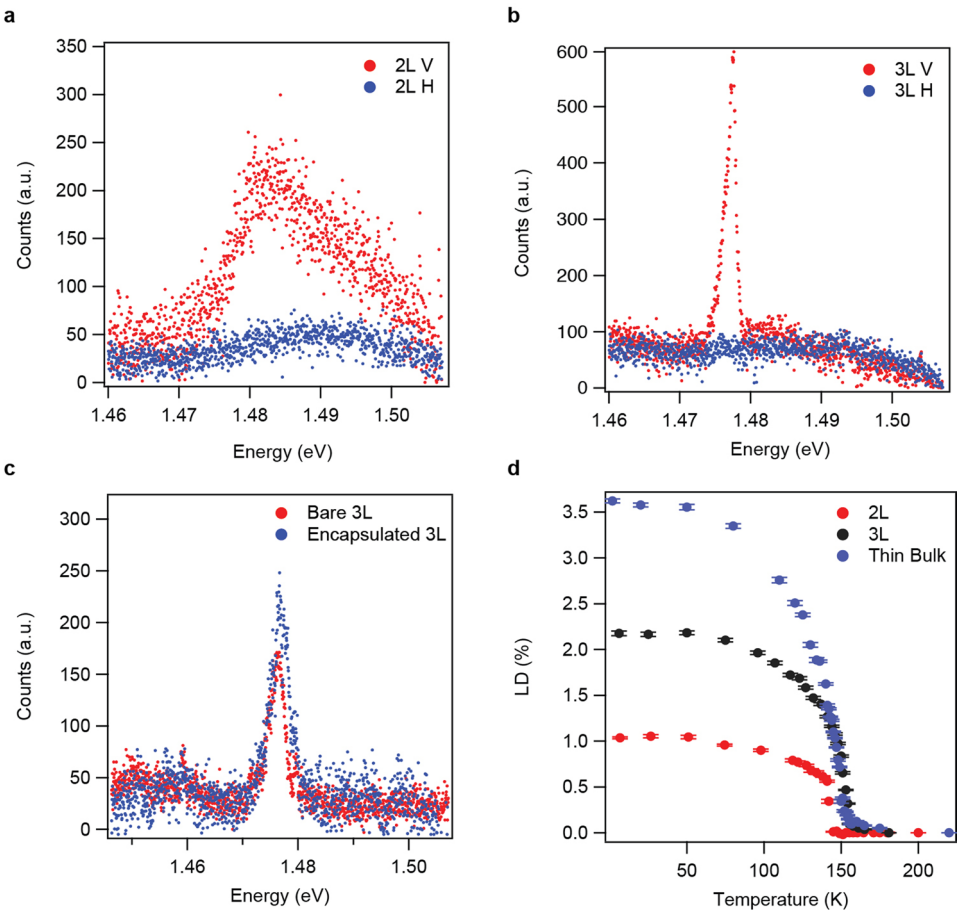

Extended Data Fig. 6 | Additional measurements of atomically thin samples. Polarization resolved photoluminescence spectra of **a**, bilayer and **b**, trilayer at 15 K. **c**, Comparison of the photoluminescence spectra with and without hBN encapsulation of a trilayer. There is no appreciable linewidth difference between the two. **d**, Temperature dependent linear dichroism of bilayer, trilayer, and thin bulk crystal. Error bars were obtained from a sinusoidal fit of the rotational LD measurements.

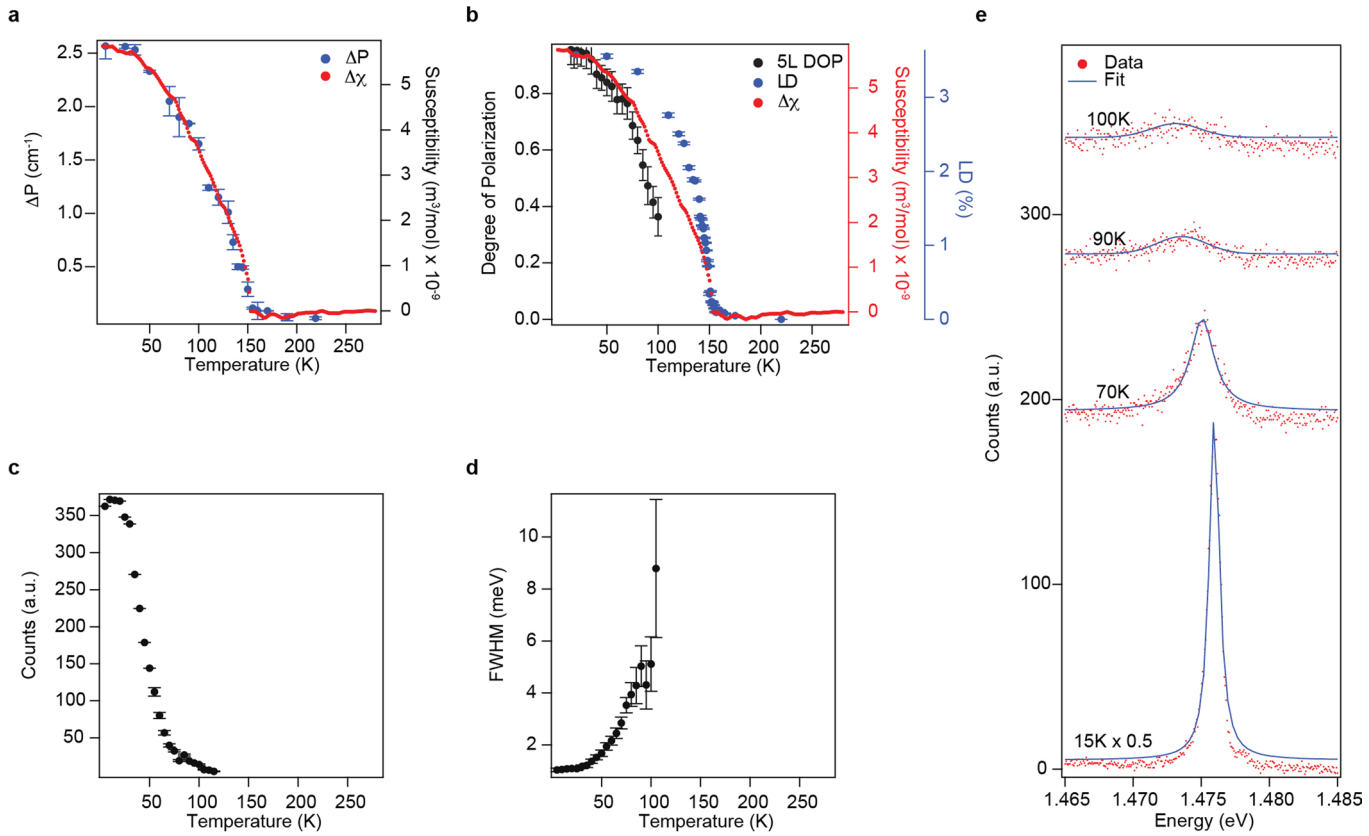

Extended Data Fig. 7 | Comparison of temperature dependent optical properties of a five-layer sample with in-plane magnetic susceptibility anisotropy $\Delta\chi$ of bulk crystal $NiPS_3$. **a**, Temperature dependent energy splitting ΔP of the 180 cm^{-1} Raman mode. ref. [21] shows that ΔP can be used to probe the zigzag antiferromagnetic order. Here, we compare ΔP with $\Delta\chi$. Remarkably, both physical quantities share similar temperature dependent behavior. This comparison shows that ΔP originates from $\Delta\chi$, and $\Delta\chi$ in five-layer sample is similar to that of the bulk crystal. Error bars were obtained from a Lorentzian fit of the Raman peaks. **b**, Temperature dependent degree of linear polarization (DOP) and linear dichroism (LD) overlaid with $\Delta\chi$. Both DOP and LD resemble $\Delta\chi$, although DOP are limited below 100 K due to the vanishing photoluminescence above 100 K. **c**, Temperature dependent photoluminescence intensity and **d**, full width at half maximum (FWHM). Error bars in figures **c** and **d** represent the confidence bounds of a Lorentzian fit. **e**, Photoluminescence spectra and their respective Lorentzian fits at select temperatures.

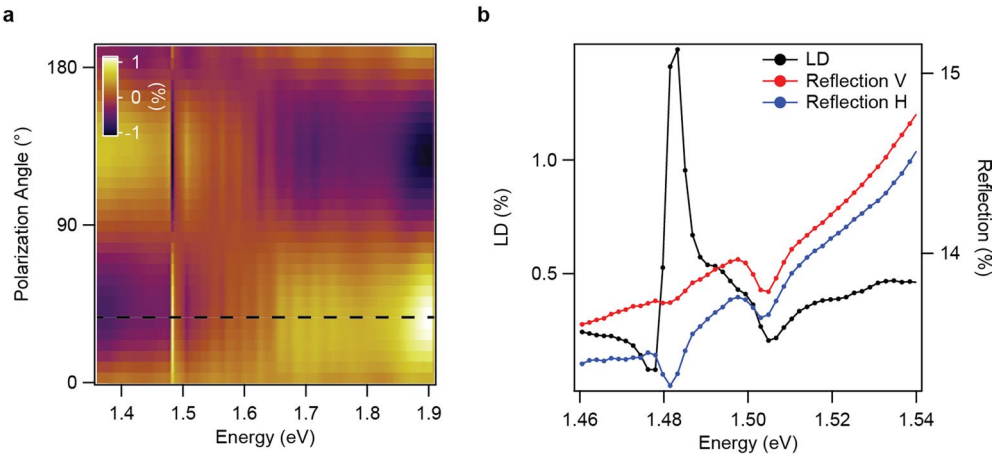

Extended Data Fig. 8 | Polarization-resolved optical reflection and its connection to linear dichroism spectrum. a, Polarization dependent linear dichroism (LD) spectra. Black dashed line corresponds to LD presented in Fig. 4a (main text), which is obtained by the excitation along the vertical axis. **b**, Red and blue curves are vertically and horizontally polarized optical reflection spectra, overlaid with the LD spectrum (black curve). Two resonances are observed[30]. The low energy resonance near 1.4815 eV has much stronger polarization dependence than the one near 1.504 eV. The difference of these two peaks partially contribute to the observed LD lineshape.

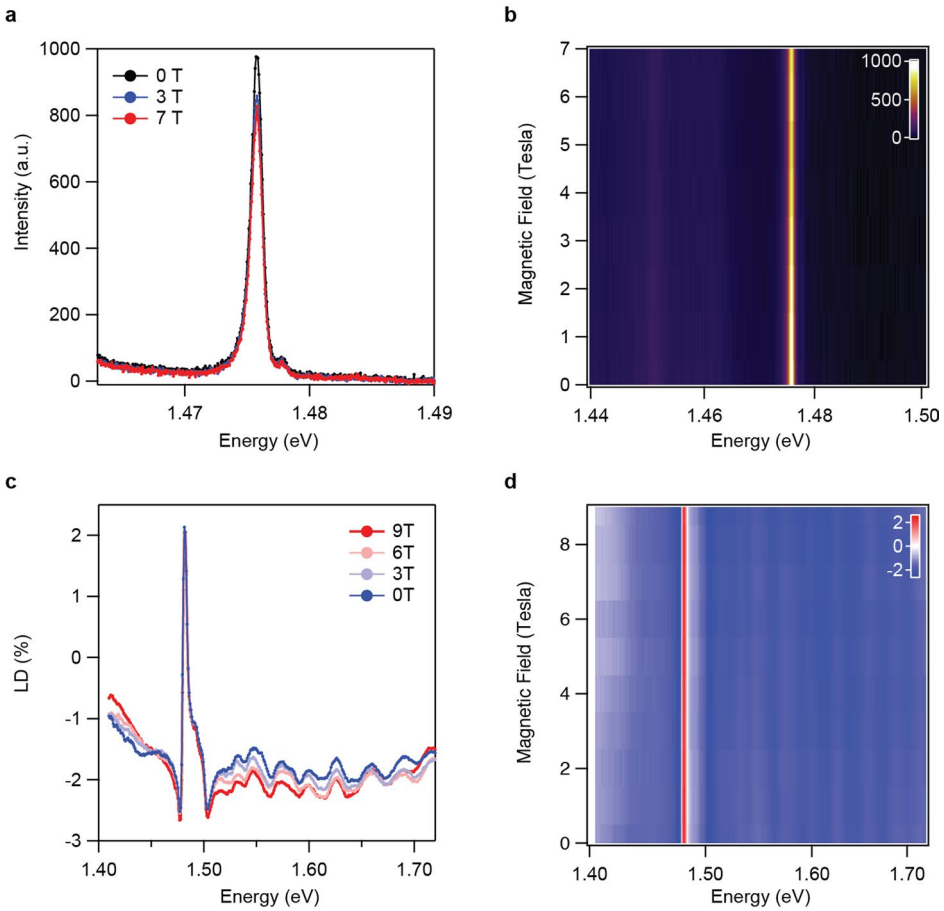

Extended Data Fig. 9 | Magnetic-field dependent photoluminescence and linear dichroism. a, Photoluminescence spectra of a five-layer sample at selected magnetic fields. **b**, Photoluminescence intensity plot of the same 5L sample as a function of magnetic field and photon energy. **c**, LD of a bulk crystal at selected magnetic fields. **d**, LD intensity plot as a function of magnetic fields and photon energy. All experiment data are taken at 15 K.